Research Square

Preprints are preliminary reports that have not undergone peer review.
They should not be considered conclusive, used to inform clinical practice,
or referenced by the media as validated information.

Microscopic stress concentration of salt crystallization damage on the surface of cement-based materials: Simulation characterization and machine learning analysis

Xuefeng Liu
Shandong Agricultural University
Ze Zhang
Shandong Agricultural University
Jinbo Yang
yangjinbo@tsinghua.org.cn

Shandong Agricultural University
Siqi Li
Chongqing University
Zhenhua Huang
Zhengzhou University
Jinpeng Zhang
Shandong University of Science and Technology

Research Article

Keywords: Cement paste, Durability, Salt crystallization, Crystallization damage, Stress concentration

Posted Date: November 19th, 2026

DOI: https://doi.org/10.21203/rs.3.rs-11767243/v1

License: This work is licensed under a Creative Commons Attribution 4.0 International License.
Read Full License

Additional Declarations: No competing interests reported.

Microscopic stress concentration of salt crystallization damage on the surface of cement-based materials: Simulation characterization and machine learning analysis

Xuefeng Liu[1], Ze Zhang[1], Jinbo Yang[1]*, Siqi Li[2], Zhenhua Huang[3], Jinpeng Zhang[4]

1. College of Water Conservancy and Civil engineering, Shandong Agricultural University, Tai'an, Shandong, 271018, P. R. China

2. School of civil Engineering, Chongqing University, Chongqing, 400045, P. R. China

3. School of Water Conservancy and Transportation, Zhengzhou University, Zhengzhou, Henan, 450001, P. R. China

4. College of Resources, Shandong University of Science and Technology, Tai'an, Shandong, 271001, P. R. China

*Corresponding author: Dr. Jinbo Yang, Email address: yangjinbo@tsinghua.org.cn

Abstract: The salt crystallization pressure is an important effecting factor for the physical salt corrosion of cement-based materials. However, considering complex micropore structures and different material boundary conditions, the evolution law of stress concentration in cement paste caused by the crystallization pressure has not yet been clarified. This paper focused on the confined crystallization of NaCl within the micropores of hardened cement paste. Two-dimensional dual-pore FEA models considering the micropore structures and different material boundary conditions were established. The effects of micropore and crystal morphology, crystallization pressure, infilling degree, pore spacing, and boundary condition on the maximum tensile stress were numerically simulated and analyzed. In addition, a FEA-driven machine learning dataset was constructed, and maximum tensile stress machine learning models were established using RF, XGBoost, and BPNN methods. Further, by integrating SHAP, PDP, and MRA, the main controlling factors were quantified and nonlinear interactions were identified. Taken together, the findings show that the stress concentration induced by salt crystallization is not solely determined by the crystallization pressure, but is influenced by the pore geometry, crystal infilling degree, and the boundary condition. The

crystallization pressure generates a significant local tensile stress concentration at the end of the micropore's long axis. When micropore is fully infilled, the maximum tensile stress in the cement paste caused by the salt crystallization pressure can reach 17.88 times the crystallization pressure. The maximum tensile stress increases with the increase of pore aspect ratio and crystallization pressure, and shows a significant nonlinear growth with the infilling degree; in contrast, the crystal aspect ratio and boundary length have a relatively weak influence. The results of machine learning interpretation further indicate that the type of boundary conditions and the degree of infilling are the main sensitive factors, and at the same time, high infilling degree shows a significant synergistic effect with high crystallization pressure. The BPNN method achieved the best prediction performance, with a R^2 of 0.992, RMSE of 0.302 MPa, and MAE of 0.148 MPa. The FEA-driven machine learning framework established provides a new analytical method for the quantitative characterization of micropore-scale salt crystallization stress concentration and the evaluation of physical salt corrosion damage in cement-based materials.

Keywords: Cement paste; Durability; Salt crystallization; Crystallization damage; Stress concentration

1. Introduction

Durability issues of structural buildings in coastal and saline environments have become one of the major challenges currently facing the field of sustainable civil engineering [1-3]. Under the aforementioned environmental conditions, cement-based materials are subjected to prolonged exposure to saline solution infiltration and moisture migration. Influenced by periodic wetting-drying cycles, wind-blown, and freeze-thaw cycles, the pore solutions in cement-based materials gradually reach supersaturation, leading to salt crystallization. As crystals form under confining from micropore walls, crystallization pressures are generated, resulting in internal stress accumulation, microcrack formation, and deterioration of durability, severely decreasing the safety and resilience of structural building systems [4-8]. Therefore, studying the influence of salt crystallization pressure on the salt corrosion damage of cement-based materials holds significant theoretical value and practical significance for ensuring the long-term safe operation of structural buildings in coastal and saline environments.

The literature indicates that, from the view of research methods, the studies on the deterioration of cement-based materials caused by salt crystallization can be broadly classified into two categories: experimental research and numerical simulation research [9-11]. The experimental research is relatively extensive. The existing studies mainly use methods such as salt solution immersion, partial immersion, wetting-drying cycling, and microstructure characterization to analyze the migration of salt, crystal precipitation, and the evolution laws of the macroscopic and microscopic properties of the cement-based materials. Lee and Kurtis [12] adjusted the water-to-cement ratio and the amount of nanoparticles to control the micropore structure of cement-based materials. They found that the degree of salt crystallization damage was closely related to the pore size distribution and pore structure characteristics, indicating that the microscopic pore structure of the material has a significant regulatory effect on the crystallization damage. Jiang et al. [13] discovered through partial immersion experiments that the concentration of chlorides could alter the location and spatial distribution of sulfate crystals, thereby affecting the crystallization pressure and the surface erosion degree of cement-based materials. Sun et al. [14] pointed out that different exposure to wetting-drying cycling conditions would significantly alter the salt transport and crystallization location. Among them, continuous capillary liquid supply and surface evaporation are more likely to cause local salt

concentration, crack formation, and degradation of cement-based material mechanical properties. Yang et al. [15] proposed a continuous two-stage physical model of "latent stage - degradation stage" through artificial sea salt accelerated wetting-drying cycling experiments. They found that the early salt crystal infilling could temporarily improve the macroscopic properties of the mortars, but as the confined crystallization continued to develop, the tensile stress induced by the crystallization pressure kept increasing and eventually led to the rapid expansion of microcracks in cement-based materials. Based on the experimental researches, some scholars further employed theoretical analysis and numerical simulation methods to study salt transport, crystal growth, crystallization pressure and the resulting mechanical responses. Zhang et al. [16] established a coupled model of transport-chemistry-physics-mechanics considering the effects of wetting-drying cycles, linking the pore solution concentration, crystallization pressure and material stiffness degradation. This model enabled the prediction of the expansion and damage evolution during external sulfate erosion. At the micropore scale, Zhang et al. [17] established a finite element model for the confined crystallization of NaCl within the micrometer-sized pores of hardened cementitious materials. They found that a significant tensile stress concentration occurred at the end of the pore's long axis during crystallization, and the local maximum tensile stress could reach several times the applied crystallization pressure. In recent years, with the rapid development of micro-scale mechanics, Lo Presti et al. [18] pointed out that if only the macroscopic tensile strength of the material is used to judge the salt crystallization damage, the influence of the mechanical confining at the micropore scale might be overlooked. They explicitly considered the confining effect of the crystal crystallization pressure acting on the micropore walls and the surrounding materials through a multi-scale model.

Together these studies provide important insights into the fundamental mechanisms of salt crystallization and the resulting macroscopic performance degradation of cement-based materials. It also clarifies that crystallization-induced pressure can generate significant tensile stress concentrations around micropores, and the relatively low tensile strength of cement-based materials makes this localized stress a key factor in salt crystallization damage. However, there is currently a lack of quantitative understanding regarding how crystallization pressure influences the evolution of local maximum tensile stress under complex micropore structures and various material boundary conditions. Much uncertainty still exists about the relationship between the material structure and macroscopic properties, which is an enormous knowledge gap needed to be filled with long-term and

continuous researches. The internal micropores of cement-based materials exhibit heterogeneity. Different internal crystal morphologies, crystal infilling degrees, micropore structure, and material boundary conditions may all alter the transmission path of crystallization pressure and the local stress distribution. From this, it can be seen that considering only a single factor such as crystallization pressure or pore parameters is insufficient to effectively explain the local mechanical response generated by salt crystallization. Therefore, it is urgent to establish a model framework that encompasses multiple factors such as micropore structure, crystal infilling degree, and material boundary conditions, and to quantitatively study the independence and interaction of different factors on the maximum tensile stress.

Furthermore, the numerical simulation research method can effectively overcome the limitation that the internal stress is difficult to measure directly in experiments, providing a foundation for studying the relationship between crystallization pressure and local stress concentration. To describe the local stress field under complex pore geometries and boundary conditions, and to reveal the stress concentration induced by salt crystallization, it offers an effective means [19-22]. However, finite element analysis usually adopts a single-factor variation approach, which is unable to accurately depict the nonlinear coupling and interaction effects among multiple variables. Meanwhile, as the number of parameters increases, the cost of large-scale finite element calculations also rises significantly. Machine learning models can learn the complex mapping relationship between multiple input parameters and mechanical responses from finite element data, and achieve rapid predictions with lower computational costs [23-26]. The combination of finite element numerical simulation and machine learning has provided a new approach for the study of the salt corrosion effect of crystallization pressure.

Based on this, this article took the constrained crystallization of sodium chloride (NaCl) within the micropores of hardened cement paste as the research object, established a two-dimensional dual-pore finite element analysis (FEA) model considering different boundary conditions, and studied the effects of pore aspect ratio, crystal aspect ratio, crystallization pressure, infilling degree, pore spacing and boundary size on the maximum tensile stress; In addition, a FEA-driven machine learning dataset was constructed, and maximum tensile stress machine learning models were established using Random Forests (RF), eXtreme Gradient Boosting (XGBoost), and Back Propagation Neural Network (BPNN). Further, by integrating SHapley Additive exPlanations (SHAP), Partial

Dependence Plot (PDP), and Multi-factor Response Analysis (MRA), the main controlling factors were quantified and nonlinear interactions were identified. By establishing a quantitative connection between crystallization, micropore structure, boundary conditions and local tensile stress response, the main controlling mechanism of local stress concentration induced by NaCl crystallization at the micropore scale can be revealed. This can provide a theoretical basis for the prediction and evaluation of salt crystallization damage in cement-based materials.

2. Methods

2.1. FEA modeling process

2.1.1. Physical description of NaCl crystallization in micropore

The concentration of NaCl solution within the micropores of cement-based materials changes with specific external environmental variations. When the solution concentration increases until it becomes supersaturated, sodium and chloride ions begin to aggregate and form crystals. The crystallization physical process of NaCl in the micropores can be roughly divided into three stages: nucleation, free crystallization, and confined crystallization, as shown in Fig. 1 [17]. When the NaCl crystal grows to come into contact with the pore wall, the crystal is confined by the pore wall, and a crystallization pressure is generated at the contact area between the crystal and the micropore wall. This crystallization pressure acts on the pore wall and further causes local deformation and stress concentration of the hardened cementitious material, thereby resulting in damage. During the confined crystallization stage, crystallization pressure will be generated through the confined crystallization surface and the confined crystallization surface area will increase with the infilling degree increasing. The following FEA modeling is based on the assumed confined crystallization stage.

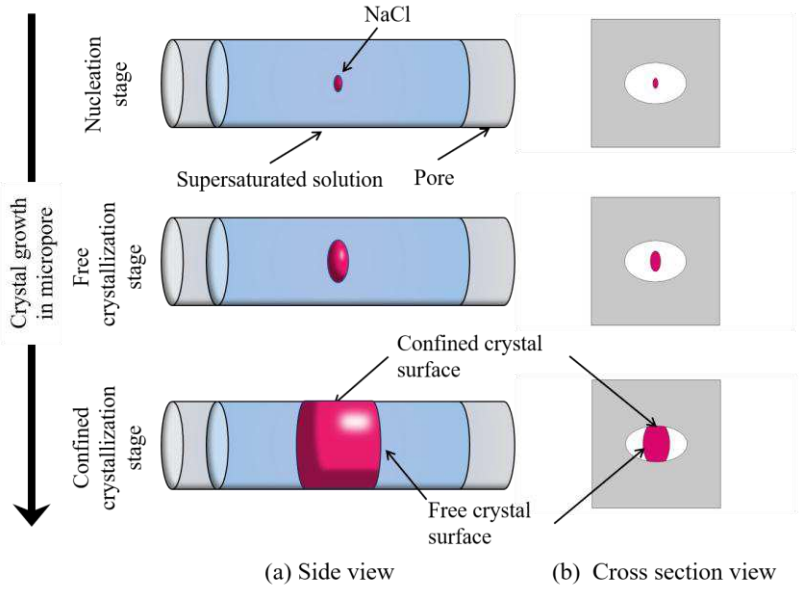


Fig. 1. Schematic diagram of the crystallization process of NaCl in micropores [17].

2.1.2. FEA modeling for NaCl crystal and cement paste

A two-dimensional plane model of NaCl confined crystallization within micropores of hardened cement paste was established using COMSOL Multiphysics 6.0 as shown in Fig. 2. Based on experimental observations from relevant studies [27–29], the micropore shape of hardened cement paste was modeled as elliptical. For hardened cement paste, the model unit dimensions were set to 7 μm × 4 μm, as shown in Fig. 2(a). Naillon et al. [30] found through micropipette evaporation experiments that the shape of NaCl crystals during evaporation crystallization is approximately elliptical. Therefore, the NaCl crystal model also adopted an elliptical shape, as shown in Fig. 2(b). The width of the elliptical shape micropore (W_{pore}) and the initial length of the elliptical NaCl crystal ($W_{crystal}$) were both set as 1 μm. The width of the elliptical shape micropore (L_{pore}) was set as a variable in the subsequent analysis.

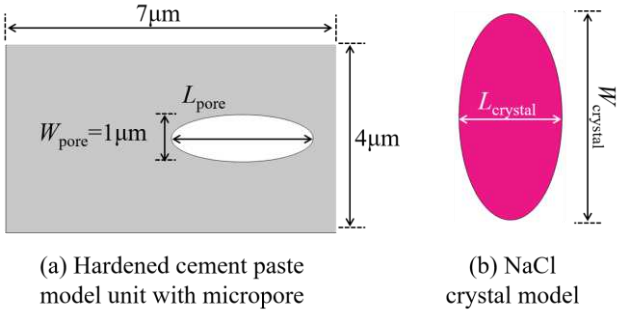


Fig.2. Two-dimensional plane FAE models.

Furthermore, to study the interactions between micropores, two single-pore models were combined to construct a dual-pore FEA model, as shown in Fig. 3. The model consisted of two parts which were hardened cement paste and NaCl crystal. Both were assumed to be homogeneous and isotropic materials. The elastic modulus of the hardened cement paste was set as 25.00 GPa, the Poisson's ratio was 0.25, the density was 1950.00 kg/m³, the ultimate tensile strength was 2.67 MPa, and the ultimate compressive strength was 35.00 MPa [31-33]. The elastic modulus of NaCl crystal was set as 25.20 GPa, the Poisson's ratio was 0.37, the density was 2160.00 kg/m³, the ultimate tensile strength was 1.50 MPa, and the ultimate compressive strength was 34.70 MPa [34]. All the materials adopted the linear elastic constitutive relationship. The main analysis focused on the local stress response around the micropores under the action of crystallization pressure. For the dual-pore model, the length (L_b) and width (W_b) were 7 μm and 4 μm relatively. The micropore spacing (D_p) was set as a variable in the subsequent analysis.

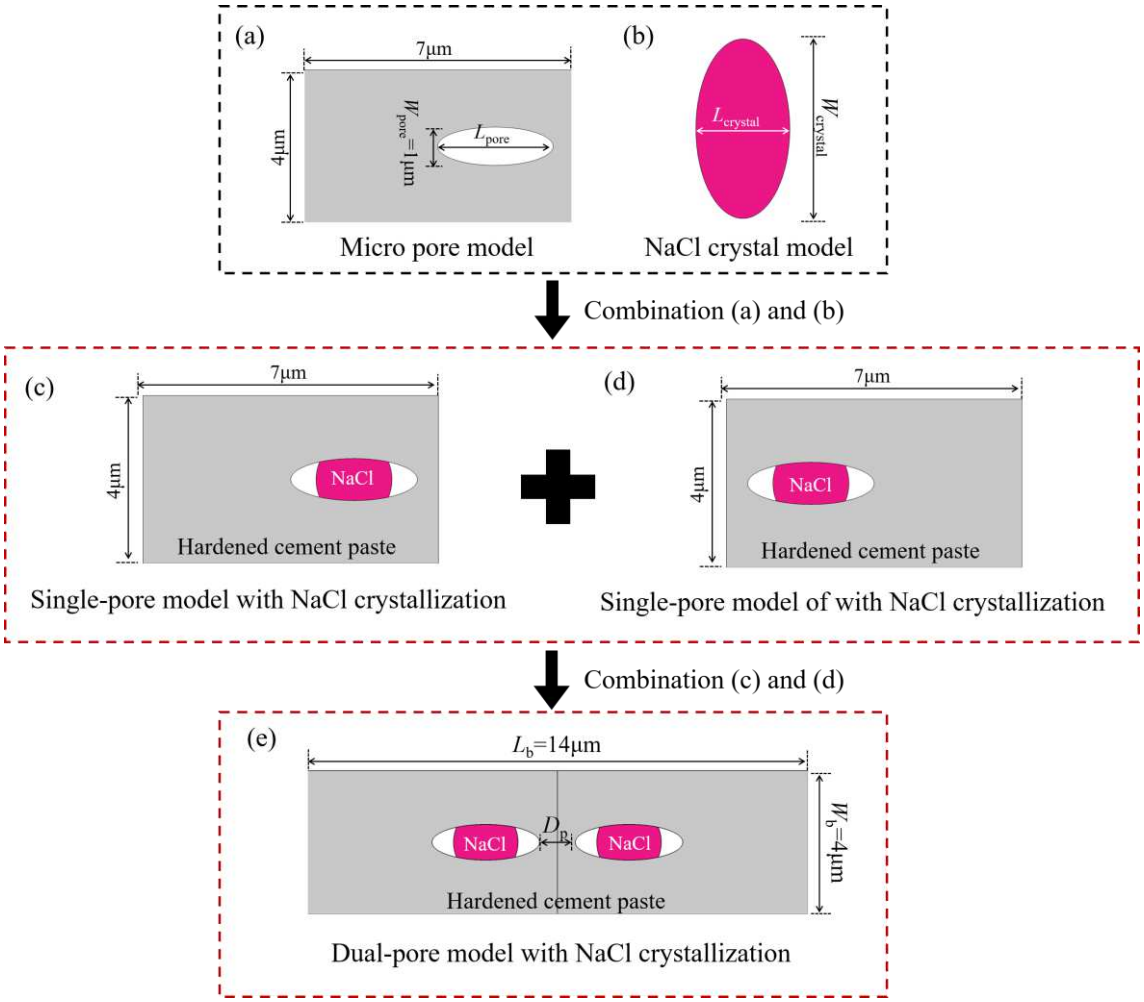


Fig. 3. Two-dimensional plane dual-pore FEA modelling for NaCl crystallization in hardened cement paste.

2.1.3. Setting boundary conditions

The micropore structure of the surface layer of cement-based materials is usually in direct contact with the salt solution and is the area most affected by salt crystallization. Therefore, the study of the micropore structure at the surface layer was designed. The external boundary conditions imposed on the pores at different positions on the surface are also different, which leads to variations in the crystallization damage effects [35]. To study the influence of external boundary conditions on crystallization stress concentration, four boundary conditions were set for the dual-pore model, namely the internal boundary condition (B_i), the side surface boundary condition (B_s), the front surface boundary condition (B_f), and the corner boundary condition (B_c), as shown in Fig. 4. For B_i, all outer boundaries were set as being fixed. For B_s, the one side outer boundary was set as being free. For B_f, the front outer boundary was set as being free. For B_c, two adjacent outer boundaries were set as being free. The above boundary conditions were used to characterize the degree of constraint exerted by hardened cementitious materials on pore deformation at different spatial locations.

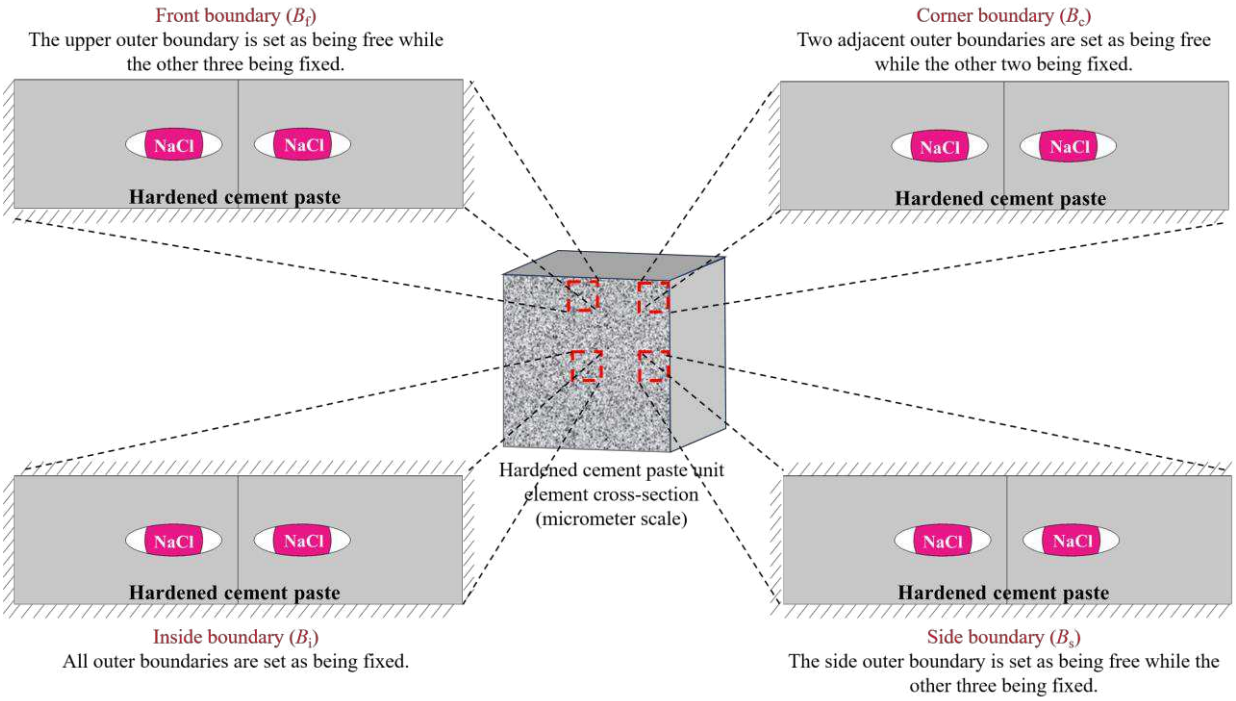


Fig. 4. The boundary conditions setting for the dual-pore FEA model.

2.1.4. Parametric design

Assuming that the crystallization pattern of NaCl at the micrometer pore level is consistent, when the salt solution concentration reaches supersaturation, salt crystals will form, and eventually crystallization pressure is generated on the interface between crystal and micropore wall. Therefore, the five aspects of pore geometry, crystal morphology, crystallization pressure, pore interaction and boundary condition are the key influencing factors for exploring the crystallization stress concentration. Based on the above analysis, this article selected parameters such as pore axial ratio A_{pore} (L_{pore}/W_{pore}), crystal axial ratio $A_{crystal}$ ($L_{crystal}/W_{crystal}$), crystallization pressure P_c, pore spacing D_p, boundary length L_b, boundary width W_b, and infilling degree I defined as equation (1) for parametric analysis. Among them, A_{pore} represents the micropore morphology; $A_{crystal}$ represents the crystal morphology of NaCl; P_c represents the force applied to the pore wall during the confined growth of the crystal; D_p is used to evaluate the mutual influence between the stress fields of adjacent micropores; L_b and W_b represent the model scale and the constrained range of the material around the micropores; I represents the infilling degree of the crystal in the pores, and by combining different boundary conditions, the local stress concentration was investigated.

$$I = \frac{S_c}{S_p} \tag{1}$$

Where, S_c and S_p represent the cross-sectional area of NaCl crystal and the cross-sectional area of the pore, respectively, μm^2.

Based on the relevant literature [27, 36, 37], a single-factor parametric analysis was conducted. The parameters were changed separately to study their effects on the maximum tensile stress. The parameters setting in numerical simulation is shown in Table 1. The A_{pore} was set at 2.0, 3.0, 4.0 and 5.0; $A_{crystal}$ were set at 0.2 and 1.2; the P_c was set at 0.46, 0.92, 1.38 and 1.84 MPa; D_p was set at 0.5, 1.0, 1.5 and 2.0 μm; L_b was set at 14, 24, 34 and 44 μm; W_b was set at 4, 9, 14 and 19 μm. For the infilling degree I, first, the corresponding geometric shape was determined based on A_{pore} and $A_{crystal}$. Then, the crystal-pore overlapping area was obtained through Boolean operations, and four infilling degrees of 0.25, 0.50, 0.75, and 1.00 were selected for analysis. For each set of parameters, the mechanical responses under four different boundary conditions were calculated separately.

Table 1

Parameters setting in FEA numerical simulation.

A_{pore}	$A_{crystal}$	P_c/MPa	D_p/μm	L_b/μm	W_b/μm	I
2.0	0.2	0.92	1.0	14.0	4.0	1.0
3.0	0.2	0.92	1.0	14.0	4.0	1.0
4.0	0.2	0.92	1.0	14.0	4.0	1.0
5.0	0.2	0.92	1.0	14.0	4.0	1.0
3.0	0.2	0.92	1.0	14.0	4.0	1.0
3.0	1.2	0.92	1.0	14.0	4.0	1.0
3.0	0.2	0.46	1.0	14.0	4.0	1.0
3.0	0.2	0.92	1.0	14.0	4.0	1.0
3.0	0.2	1.38	1.0	14.0	4.0	1.0
3.0	0.2	1.84	1.0	14.0	4.0	1.0
3.0	0.2	0.92	0.5	14.0	4.0	1.0
3.0	0.2	0.92	1.0	14.0	4.0	1.0
3.0	0.2	0.92	1.5	14.0	4.0	1.0
3.0	0.2	0.92	2.0	14.0	4.0	1.0
3.0	0.2	0.92	1.0	14.0	4.0	1.0
3.0	0.2	0.92	1.0	24.0	4.0	1.0
3.0	0.2	0.92	1.0	34.0	4.0	1.0
3.0	0.2	0.92	1.0	44.0	4.0	1.0
3.0	0.2	0.92	1.0	14.0	4.0	1.0
3.0	0.2	0.92	1.0	14.0	9.0	1.0
3.0	0.2	0.92	1.0	14.0	14.0	1.0
3.0	0.2	0.92	1.0	14.0	19.0	1.0
3.0	0.2	0.46	1.0	14.0	4.0	0.25
3.0	0.2	0.46	1.0	14.0	4.0	0.50
3.0	0.2	0.46	1.0	14.0	4.0	0.75
3.0	0.2	0.46	1.0	14.0	4.0	1.0

2.1.5. FEA numerical simulation process and stress extraction

The finite element calculation of the NaCl crystallization process was conducted using COMSOL Multiphysics 6.0. The object was on studying the stress distribution in cement paste and the FEA numerical simulation process is shown in Fig. 5. First, to determine the corresponding geometric shape based on the crystal size. Then, to split the model. Subsequently, to apply the crystallization pressure P_c in the form of a normal load to the contact interface between the crystal and the pore wall. The pore walls that are not in contact with the crystal remain free. The four boundary conditions are respectively added as described in Section 2.1.3. The FEA model was divided

into grids using free triangular elements, and was further refined in the contact regions between crystals and pore walls. The dual-pore model consists of 2836 domain elements and 261 boundary elements, with an average mesh quality of 0.86. After the simulation calculation was completed, the first principal stress field of the hardened cement paste region was extracted and used as the target response quantity for subsequent parameter analysis and machine learning prediction.

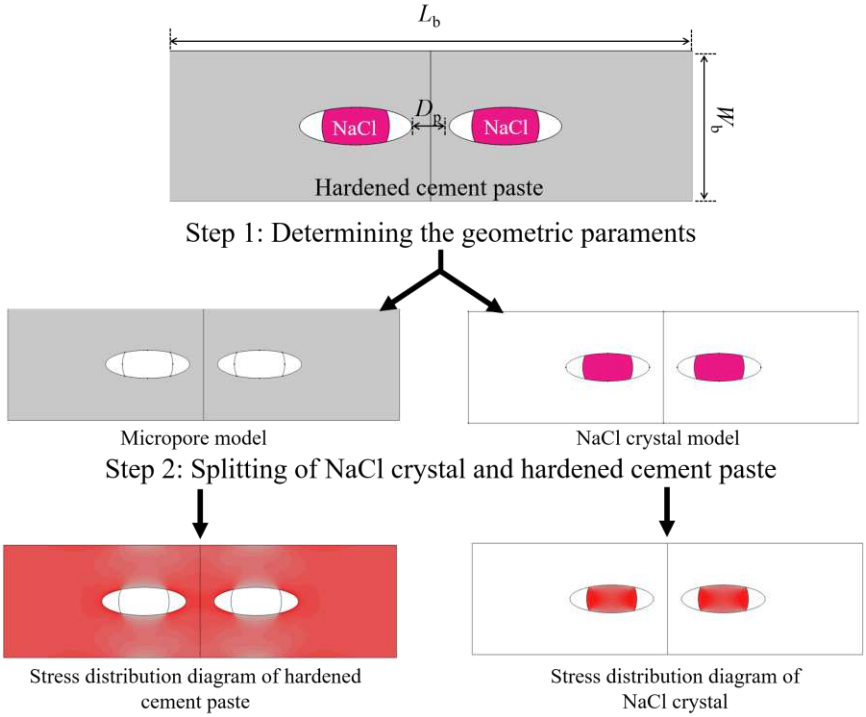


Fig. 5. FEA numerical simulation process and stress extraction.

2.2. Machine learning method

2.2.1. Construction of the finite element analysis derived database

The machine learning samples were obtained from the FEA calculation results of the aforementioned dual-pore model. Based on the finite element model, the filling degree parameter was further subdivided (into approximately 20 levels of filling degree) for finite element numerical simulation calculations. Eventually, 1008 data samples were obtained by FEA numerical simulation for machine learning.

Each data sample corresponded to a set of model input parameters and the first principal stress of the hardened cement paste calculated based on these parameters. The model input includes 7

continuous variables and 1 categorical variable, namely A_{pore}, $A_{crystal}$, P_c, D_p, L_b, W_b, I, and boundary condition type (B_i, B_s, B_f, and B_c). The first principal stress served as the prediction target for the machine learning model. To evaluate the predictive ability and generalization performance of the model, the dataset was randomly divided into a training set and an independent test set in an 8:2 ratio. The training set was used for model training and hyperparameter optimization, while the test set was only used for evaluating the final model performance. At the same time, 5-fold cross-validation was used to evaluate the stability of the model for different data divisions.

2.2.2. Machine learning models

To establish a nonlinear mapping relationship between finite element input parameters and the first principal stress, this study selected three machine learning methods—RF, XGBoost, and BPNN. Before machine learning, continuous variables were standardized using Z-score normalization to reduce the impact of different feature scales and value ranges on model training. Four boundary conditions were treated as categorical variables and converted into numerical features recognizable by the model using one-hot encoding. The hyperparameters of each model were optimized through grid search, and the optimal parameter combination was determined based on 5-fold cross-validation of the training set. After the training was completed, the prediction performance of each machine learning model was evaluated using an independent test set, and the optimal model for subsequent prediction and interpretability analysis was determined through comparison among the models.

2.2.3. Model evaluation and interpretability analysis

To evaluate the predictive capabilities of different machine learning models, the coefficient of determination (R^2), root mean square error (RMSE), and mean absolute error (MAE) were used as performance indicators. To analyze the contribution of each input parameter to the prediction results, the SHAP method was employed to explain the selected machine learning model. By calculating the SHAP values of each feature, the contributions of pore geometry, crystallization state and boundary conditions to the model output were quantified, and the global importance of each factor was evaluated based on the average absolute SHAP value. The PDP method was employed to analyze the marginal response relationship between the main input variables and stress, aiming to identify the

changing trends of each factor and the possible characteristic thresholds. Further a two-dimensional response surface for the main variables was constructed to characterize the nonlinear response and interaction of the maximum tensile stress when multiple factors change together.

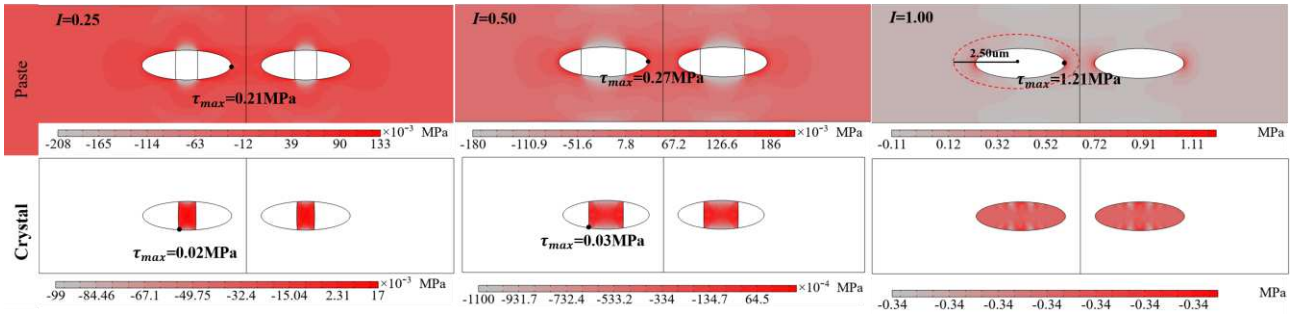
3. Results and analysis

3.1. Stress concentration phenomenon results based on FEA

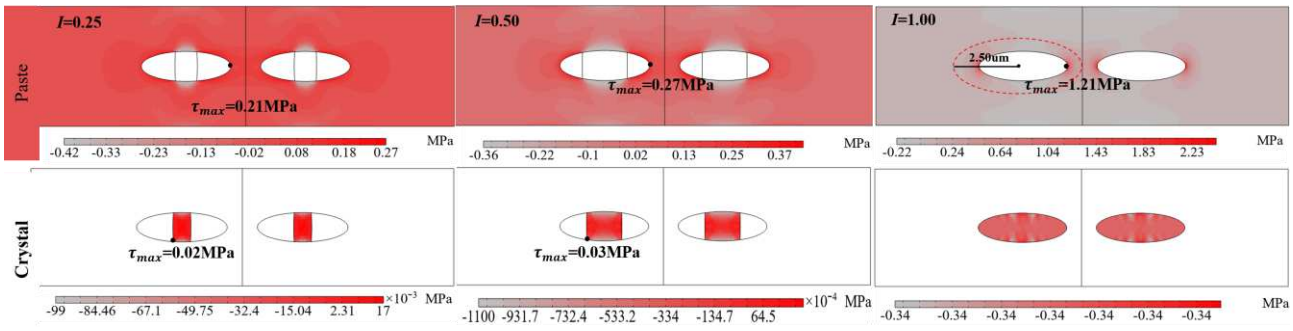
3.1.1. Crystallization-induced stress concentration around micropores

To study the distribution pattern of the first principal stress within cement paste caused by crystallization pressure, taking the one model (A_{pore}=3.0, $A_{crystal}$=0.2, P_c=0.46 MPa, D_p=1.0μm, L_b=14.0μm, W_b=4.0μm) as an example, three typical infilling degrees (I = 0.25, 0.50, 1.00) were selected. The first principal stress distribution diagrams of the cement paste and NaCl crystals were drawn, as shown in Fig. 6. As can be seen from the Fig. 6 (a) - (d) corresponding respectively to different boundary conditions, around the micro-pores at different positions, the crystallization of NaCl led to the emergence of extensive tensile areas within the surface layer. The maximum tensile stress (τ_{max}) increased with the increase in infilling degree, and the most dangerous point occurs at the vertex of the long axis end of the pore. When the I was 1.00, the maximum tensile stress under the B_i and B_s conditions was 1.21 MPa, which is approximately 2.63 times the P_c; under the B_f and B_c conditions, it was 3.84 MPa and 3.88 MPa respectively, corresponding to 8.35 times and 8.43 times the P_c. The models under B_f and B_c with more free boundaries exhibited more significant local tensile stress concentration. From the perspective of spatial distribution, the tensile stress areas within the surface layer of cement paste are mainly concentrated within a radial distance of 1.00 μm from the pore surface. The NaCl crystals were mainly subjected to compression, and the tensile stress they experience was very small. This indicates that the hardened cement paste surface layer undergoes significant tensile stress during the salt crystallization process, with the maximum tensile stress reaching 8.43 times the crystallization pressure. The tensile stress concentration caused by crystallization pressure is the direct cause of the failure of cement-based materials. It is worth noting that, due to the relatively small internal tensile stress generated, the NaCl crystal would not fail before the hardened cement paste. The calculation results of all 80 models were statistically analyzed. The

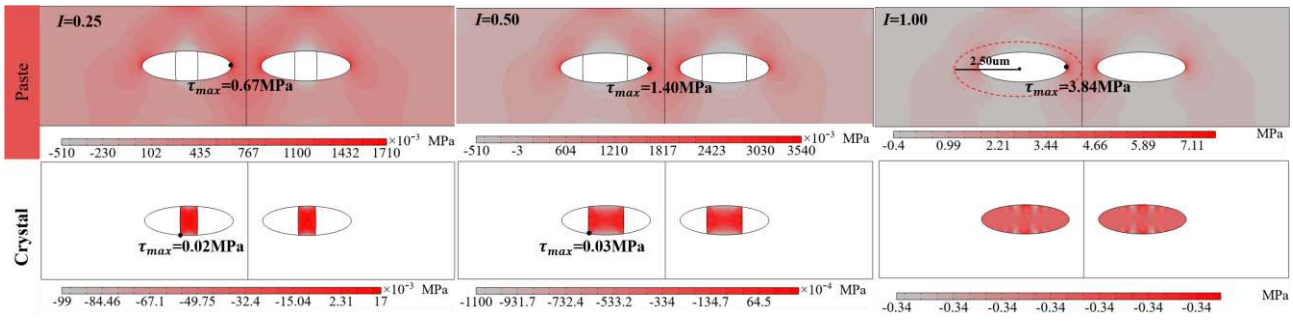
maximum tensile stress was among 0.46 to 17.88 times the crystallization pressure.



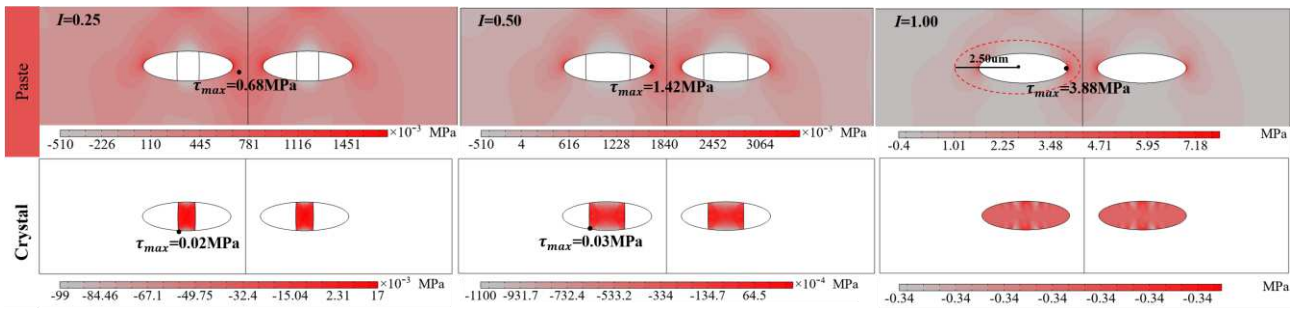
(a) B_i boundary condition



(b) B_s boundary condition



(c) B_f boundary condition



(d) B_c boundary condition

Fig. 6. Distribution patterns of the first principal stress within FEA example model (A_{pore}=3.0, $A_{crystal}$=0.2, P_c=0.46 MPa, D_p=1.0μm, L_b=14.0μm, W_b=4.0μm).

3.1.2. Effects of designed parameters on the maximum tensile stress

（a）Effects of the pore axial ratio and crystal axial ratio

Fig.7 shows the influence of A_{pore} on the τ_{max} under different boundary conditions. As the A_{pore} increased from 2.0 to 5.0, the τ_{max} under all boundary conditions showed a continuous increasing trend, indicating that the pore morphology has a significant influence on the local stress concentration caused by crystallization pressure. The larger A_{pore} corresponds to a sharper end of the long axis, thereby resulting in a more pronounced local tensile stress concentration. Under the same A_{pore}, the τ_{max} under Bi and Bs conditions was close to each other, while the results under B_f and B_c conditions were similar and overall higher. As shown in Fig. 8, the $A_{crystal}$ has a relatively weak effect on the τ_{max} compared to A_{pore}. When the $A_{crystal}$ changed from 0.2 to 1.2, the τ_{max} under various boundary conditions showed no significant change, and the stress level relationship among different boundary conditions still maintained a similar pattern to that of the A_{pore} effect analysis. Therefore, the A_{pore} is an important geometric parameter that controls the local stress concentration, while the effect of the $A_{crystal}$ is relatively limited.

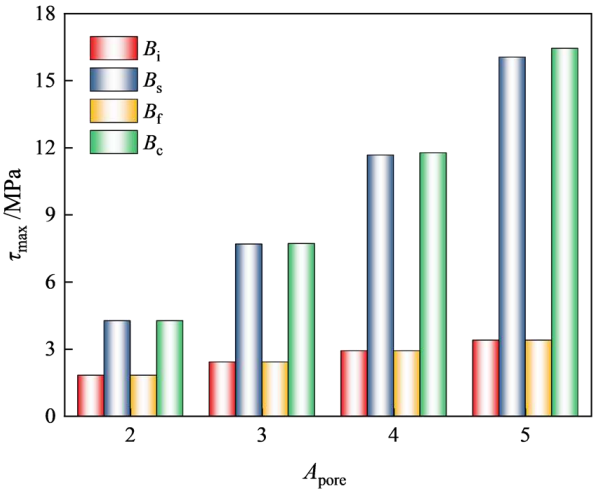


Fig. 7. Effects of A_{pore}.

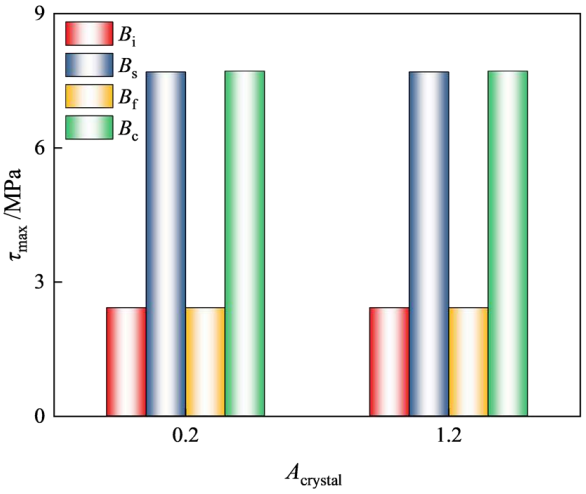


Fig. 8. Effects of $A_{crystal}$.

（3）Effects of the crystallization pressure and infilling degree

Fig. 9 shows the effect of P_c on the τ_{max} under different boundary conditions. As the P_c increased from 0.46 MPa to 1.84 MPa, the τ_{max} under each boundary condition continued to rise, showing an approximately linear growth trend overall. Under the same P_c, the τ_{max} under B_i and B_s conditions is similar, while the stress levels under B_f and B_c conditions are significantly higher. The P_c is the main factor that controls the local stress concentration level. The filling degree I also has a significant

impact on the τ_{max}. As shown in Fig. 10, as the I increased, the τ_{max} showed a non-linear upward trend overall: it grew relatively slowly in the lower infilling degree stage, and significantly accelerated in the higher infilling degree stage. This change indicates that as the crystal gradually fills the pores, the contact area between the crystal and the pore walls expands, and the local stress concentration further intensifies. Overall, the P_c mainly controls the external force intensity, while the I reflects the evolution of the load application range during the confined crystallization process. Together, these two factors determine the development level of the τ_{max}.

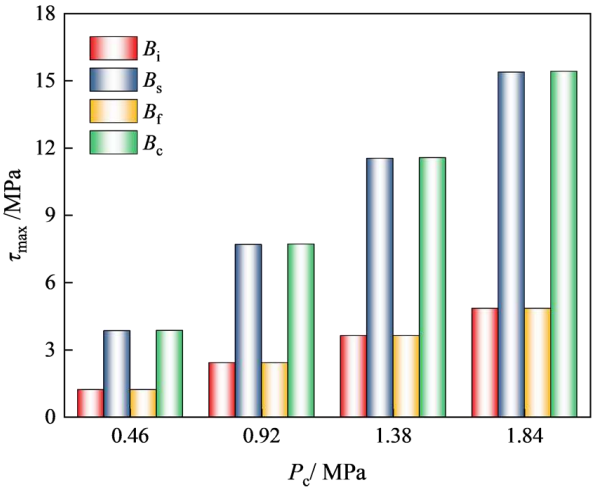


Fig. 9. Effects of P_c.

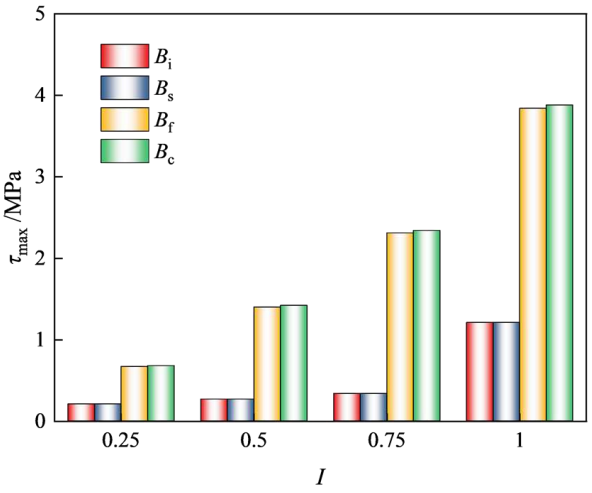


Fig. 10. Effects of I.

（3）Effects of the pore spacing, boundary length and boundary width

Fig. 11 shows the effect of D_p on the τ_{max}. When the D_p was less than 1 μm, the interaction of the stress fields between adjacent pores was significant; when the D_p exceeded 1 μm, the variation of the τ_{max} under different boundary conditions gradually slowed down, indicating that the interaction between pores had significantly weakened. As shown in Fig, 12 and 13, the boundary length L_b had a relatively small impact on the τ_{max}. The τ_{max} under different L_b were similar. In contrast, the W_b had a more significant impact on the maximum tensile stress within a smaller range of values. However, when the W_b exceeded 14 μm, its influence significantly weakened, and the τ_{max} gradually stabilized. Overall, the effect of pore spacing and boundary size on the maximum tensile stress is mainly concentrated within a relatively small scale range. When the adjacent pore spacing and model boundary size exceed a certain limit, their effect can be disregarded.

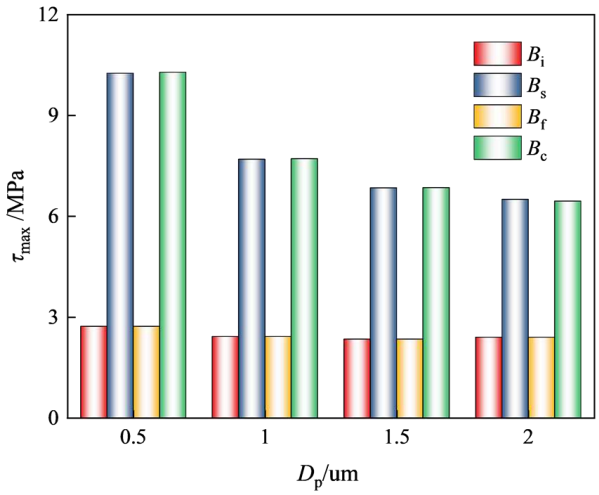


Fig. 11. Effects of D_p.

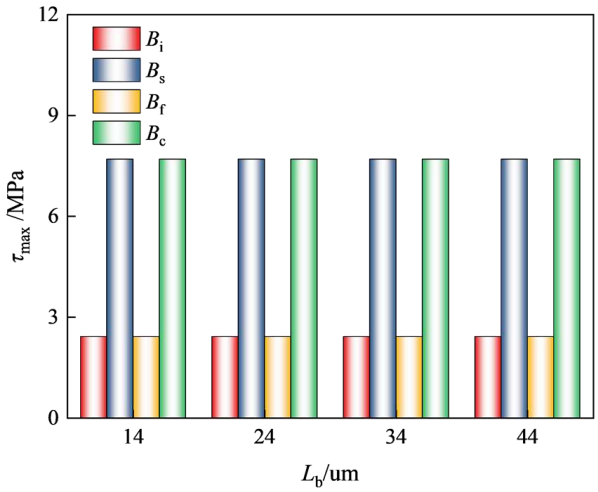


Fig. 12. Effects of L_b.

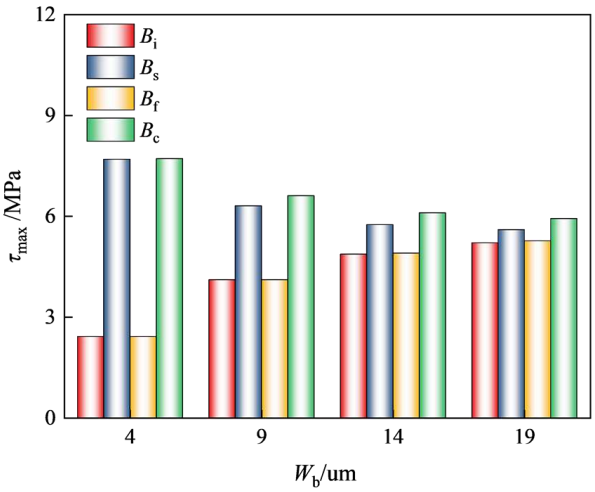


Fig. 13. Effects of W_b.

3.1.3. The maximum tensile stress calculation formula

Based on the above results, it is clearly evident that the infilling degree is the main external factor influencing the maximum tensile stress of cement-based materials. Based on the numerical simulation results, the comprehensive influence coefficients α and β were introduced to develop an empirical calculation formula for the maximum tensile stress in cement-based materials caused by crystallization in micropores, as follows:

$$\tau_{max} = \frac{P_c\left(1+\alpha I\right)}{1-\beta I} \tag{2}$$

Where, τ_{max} is the maximum tensile stress caused by crystallization in micropores (MPa), P_c is the salt crystallization pressure (MPa), α and β the comprehensive influence coefficients, I is the infilling

degree (dimensionless among 0 to 1).

For the FEA simulation data, the curve fitting function in the Origin software was used to fit this formula. The regression analysis results are shown in Table 2. The values of α and β are 0.97 and 0.70, and the R^2 is 0.79. This confirms that the empirical calculation formula for the maximum tensile stress caused by crystallization in micropores of cement-based materials has a certain degree of reliability. According to formula (2), when the infilling degree is 1.0, the maximum tensile stress value is the highest, approximately 6.57 times that of the crystallization pressure. However, this simplified analytical formula is not sufficient for accurately predicting the maximum tensile stress caused by the crystallization pressure.

Table 2

Fitting regression correlation analysis results for formula (2).

α		β		Statistics	
Value	Error	Value	Error	Reduced Chi-Sqr	Adj. R^2
0.97	0.11	0.70	0.02	0.66	0.79

3.2 Machine learning analysis

3.2.1. Performance of the machine learning models

Based on the results of the FEA numerical simulation, the prediction performance of different machine learning models on their respective test sets is shown in Table 3. The determination coefficients (R^2) of the three models all reached above 0.96, indicating that the machine learning models can effectively establish the mapping relationship between the FEA input parameters and the maximum tensile stress. Compared with the R^2 value of 0.79 for the fitting formula (2) based on the above experience, each machine learning model demonstrated better predictive capabilities. Among them, the BPNN model has the best comprehensive prediction performance. The R^2 value of the test set is 0.992, the RMSE is 0.302 MPa, and the MAE is 0.148 MPa. To verify the stability of the machine learning models, a 5-fold cross-validation analysis was conducted. The cross-validation R^2 of BPNN was 0.988 ± 0.005, that of XGBoost was 0.984 ± 0.003, and that of RF was 0.959 ± 0.008. Among them, BPNN demonstrated excellent generalization stability under different data partitions.

Based on the prediction accuracy of the comprehensive test set and the cross-validation results,

the BPNN model was selected as the machine learning model for the maximum tensile stress in the subsequent analysis. The comparison of the BPNN prediction values and the FEA calculation values is shown in Fig. 14. The overall distribution of the prediction results is close to y = x. The residual distribution of the BPNN prediction is shown in Fig. 15. Most of the residuals are concentrated around the zero value, and no significant systematic deviation is observed.

Table 3

Performance of the machine-learning models.

Machine learning model	R^2	RMSE/MPa	MAE/MPa	5-fold cross-validation R^2
RF	0.966	0.631	0.390	0.959±0.008
XGBoost	0.989	0.353	0.229	0.984±0.003
BPNN	0.992	0.302	0.148	0.988±0.005

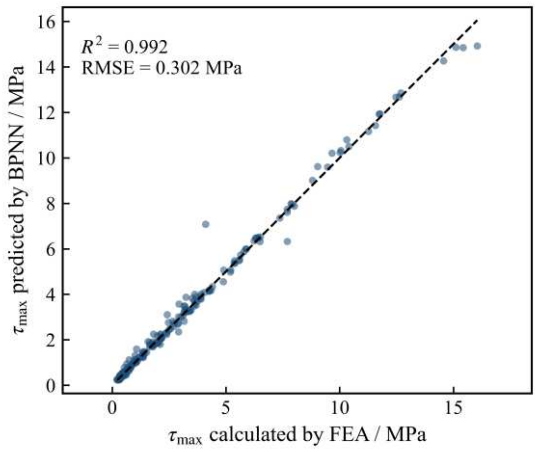


Fig. 14. Performance of BPNN model.

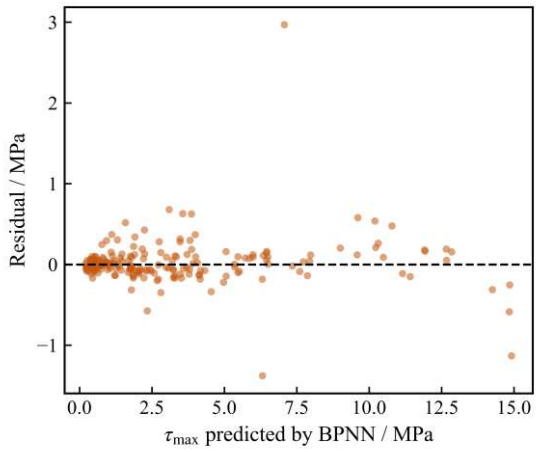


Fig. 15. Prediction residual distribution of BPNN.

3.2.2. Global feature importance analysis based on SHAP

To further identify the main controlling factors that have the greatest impact on the maximum tensile stress, the SHAP method was employed to explain the BPNN model. The distribution of SHAP values for each input parameter on the test set is shown in Fig. 16. The average absolute SHAP value is used to measure the global importance of the features, as presented in Fig. 17 and Table 4. The results show that the mean |SHAP| value for the boundary condition type is the highest, at 2.10, and its relative importance reaches 43.5%, making it the primary factor influencing the maximum tensile stress. The infilling degree was the second highest, with a mean |SHAP| value of 1.41 and a relative

importance of 29.3%. The contributions of P_c and A_{pore} are relatively close. The mean |SHAP| values are 0.51 and 0.50 respectively, and their relative importance is 10.6% and 10.3% respectively. In contrast, the influences of the boundary width W_b and the pore spacing D_p are relatively smaller, with their relative importance being 4.1% and 2.1% respectively. The mean |SHAP| value of the $A_{crystal}$ and the L_b is only 0.0008 and 0.0005 respectively, and its influence on the maximum tensile stress can be ignored. The above results indicate that the maximum tensile stress is mainly controlled by the boundary condition, infilling degree, crystallization pressure and pore geometric shape, while the influences of boundary size and crystal morphology are relatively limited. The ranking results are basically consistent with the results obtained from the FEA single-factor analysis in Section 3.1.

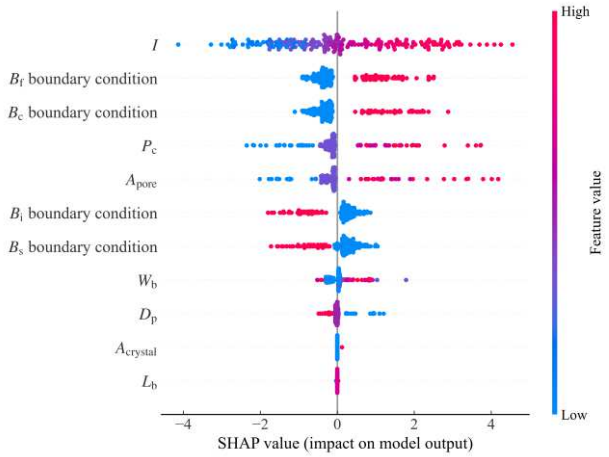


Fig. 16. SHAP feature importance distribution

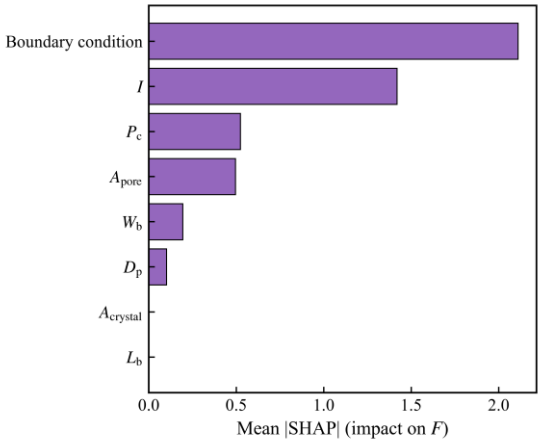


Fig. 17. SHAP feature importance bar chart

Table 4

Ranking of input parameter importance based on SHAP.

Input parameter	Mean |SHAP|	Relative importance / %
Boundary type	2.10	43.5
I	1.41	29.3
P_c	0.51	10.6
A_{pore}	0.50	10.3
W_b	0.20	4.1
D_p	0.10	2.1
$A_{crystal}$	0.0008	0.02
L_b	0.0005	0.01

3.2.3. PDP and two-dimensional response surface analysis

The partial dependence of the maximum tensile stress on the main input parameters is shown in Fig. 18 based on BPNN prediction results. The PDP is used to represent the marginal impact of a

single feature change on the model's prediction result under the condition of averaging the values of other variables. The results show that the influence of I on the maximum tensile stress is significantly non-linear. As the I increases, the maximum tensile stress continues to rise, showing a trend of being slow at the beginning and fast at the end. When the A_{pore} increases, the maximum tensile stress also continues to rise, and shows strong sensitivity in the high A_{pore} region. The P_c is linearly and positively correlated with the maximum tensile stress. This trend is consistent with the FEA results in Section 3.1. For the parameters with weaker influence, the response curves of the $A_{crystal}$ and the L_b remain basically stable; after the D_p exceeds approximately 1.0 μm, its marginal effect significantly weakens; and after the W_b exceeds 14 μm, its influence on the maximum tensile stress also tends to stabilize. The results of machine learning further verified the scale effect identified in the FEA results and its variation range.

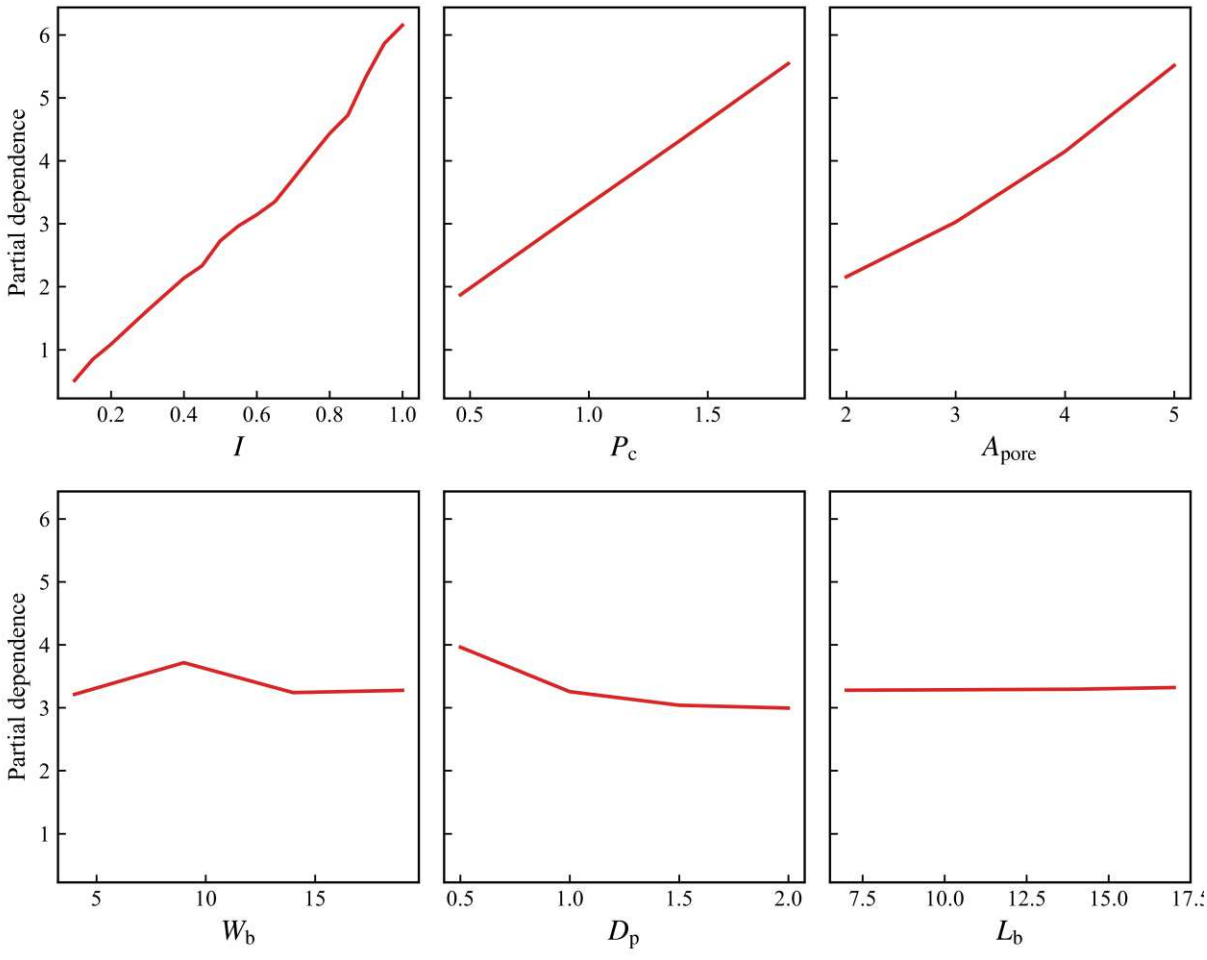


Fig. 18. Partial dependence plot for main parameters.

Based on the single-factor analysis, the interaction effects among the main variables were analyzed. Fig. 19 presents the two-dimensional response surface of the maximum tensile stress with

respect to the I and the P_c. As both increase simultaneously, the maximum tensile stress significantly rises, especially in the high infilling degree and high crystallization pressure regions, where the maximum tensile stress shows a notable nonlinear growth. This result indicates that there is a positive interaction between the infilling degree and the crystallization pressure. That is, when a higher degree of crystallization infilling and a greater crystallization pressure act together, it will further intensify the local stress concentration.

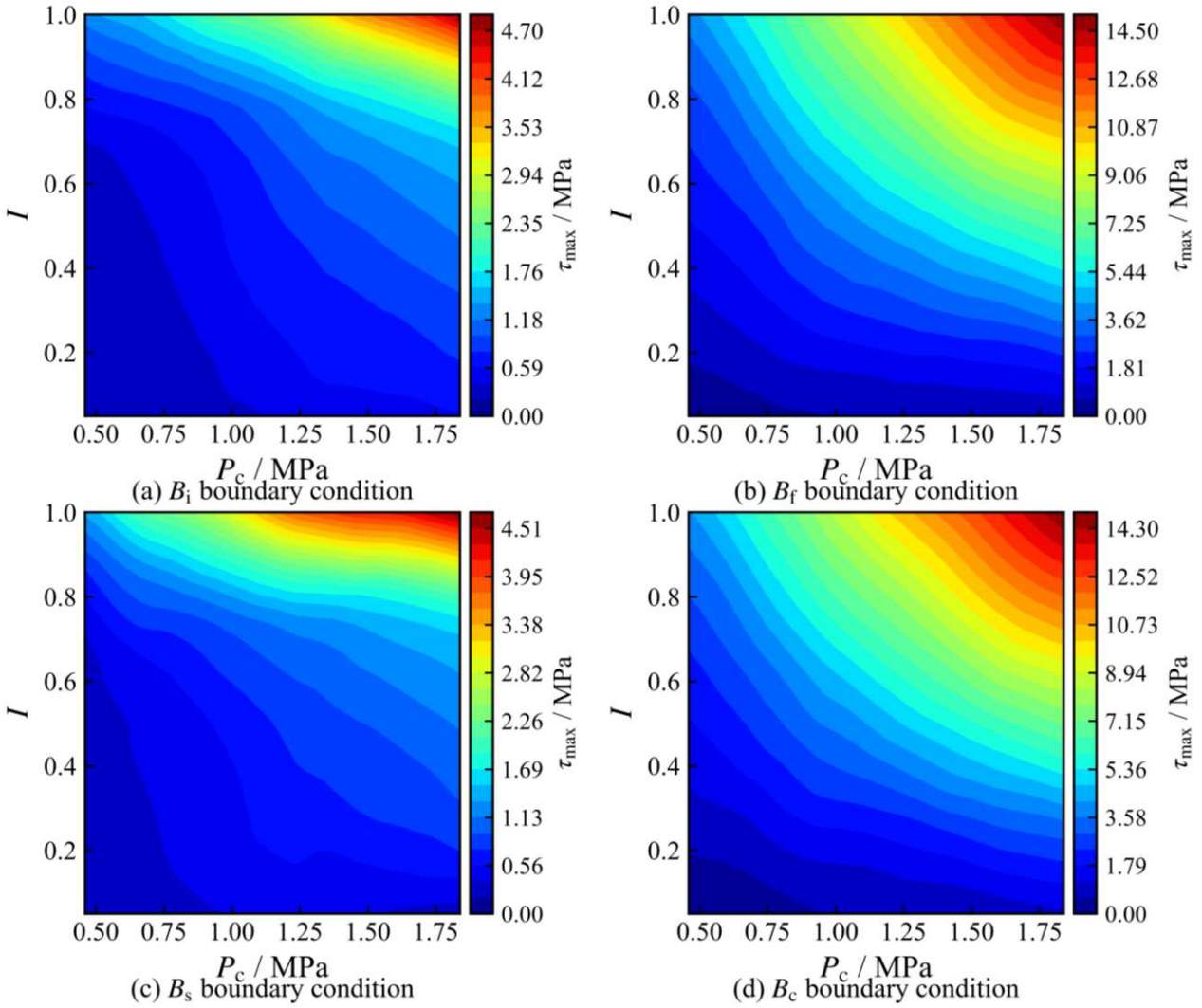


Fig. 19. The two-dimensional response surface with I and P_c.

3.2.4. Boundary condition effects on the maximum tensile stress

To further compare the stress concentration under different boundary conditions, based on the BPNN results, the variation of the maximum tensile stress under four boundary conditions was analyzed, as shown in Fig. 20. The results show that there are significant differences in the maximum

tensile stress levels under different boundary conditions. The prediction results under the B_i and B_s conditions are relatively close and overall lower, while the maximum tensile stress under the B_f and B_c conditions is similar and significantly higher than those of the former two boundary conditions. This change pattern is consistent with the results of the FEA method. The BPNN can well reproduce the significant differences in the maximum tensile stress under different boundary conditions, indicating that the boundary condition is a key factor in controlling the local stress concentration during NaCl crystallization. When the number of free boundaries increases, the maximum tensile stress rises overall. Among them, the model with a weaker constraint on the direction of the crystallization pressure shows a higher stress level. This result is in line with the result from the SHAP analysis in Section 3.2.2, which states that "the type of boundary conditions has the highest overall importance". This indicates that the influence of the boundary constraint type on the maximum tensile stress is significantly greater than that of the boundary size itself. In conclusion, the BPNN machine learning model not only can accurately predict the maximum tensile stress under different parameter combinations, but also can effectively distinguish the stress responses under different spatial constraints, providing a quantitative basis for the subsequent analysis of the salt crystallization damage mechanism in the surface layer of cement-based materials.

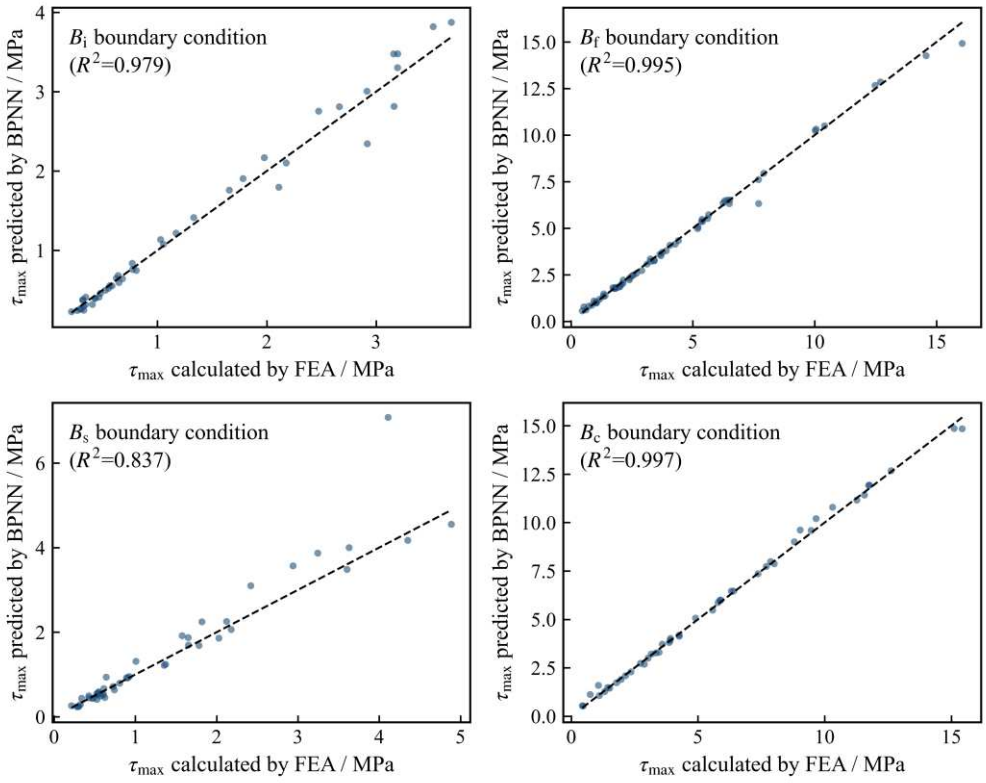


Fig. 20. Boundary condition effects on the maximum tensile stress.

4. Discussions

4.1. The mechanism of crystallization stress concentration

According to these data, we can infer that the crystallization pressure is the fundamental load resulting from the confined growth of NaCl, but it cannot directly determine the actual local tensile stress borne by the cement paste matrix. The results of this study indicate that the crystallization pressure, after being transmitted through the crystal-pore wall contact interface, causes a significant tensile stress concentration at the long axis end of the elliptical pores, and the high-stress area is mainly located in the vicinity of the pores. The results of this study indicate that the crystallization pressure, after being transferred through the crystal-pore wall contact interface, forms a significant tensile stress concentration at the long axis end of the elliptical pores. Therefore, the salt crystallization damage should be understood as a process where the crystallization pressure is redistributed within the pore structure and local stress concentration occurs, rather than the uniform transmission of the crystallization pressure throughout the material. This local magnification is mainly influenced by the shape of the bearing pore wall. An increase in the pore axis ratio makes the end of the long axis more pointed, thereby enhancing the local stress concentration, while the influence of the crystal axis ratio is relatively limited. This means that merely comparing the crystallization pressure with the macroscopic tensile strength of the material is not sufficient to determine the risk of damage. The local maximum tensile stress formed after the transformation of the crystallization pressure through the pore structure is a more direct influencing factor. It is well known that the presence of a cutout or hole in a stressed member creates highly localized stresses at the vicinity of the cutout, and the ratio of the maximum stress at the cutout edge to the nominal stress is called the stress concentration factor (SCF) [38]. It can be reasonably assumed that the SCF can be used to describe the stress concentration phenomenon caused by salt crystallization in the micropores of cement-based material, and it could be defined as the ratio of the maximum tensile stress induced by crystallization to the crystallization pressure. Future studies on the crystallization stress concentration factor (CSCF) are therefore recommended.

4.2. Boundary condition effect mechanism

The spatial constraints further controlled the above stress concentration process. Under the same pore morphology and crystalline state, different boundary conditions resulted in significantly different maximum tensile stresses; when fully filled, the CSCF could be from 0.46 to 17.88 approximately. This indicates that the position of the pores directly affects stress transmission by altering the way the surrounding matrix constrains the deformation of the pore walls.

It should be noted that this effect cannot be simply attributed to the number of free boundaries, but rather depends on the relationship between the direction of constraint release and the local deformation direction of the pores. When the mechanical constraints in the relevant direction weaken, the non-uniform deformation near the pore walls increases, thereby enhancing the stress concentration at the pore tip. The importance analysis of machine learning also shows that the influence of the type of boundary conditions is significantly greater than that of the boundary size itself. This result provides a pore-scale mechanical explanation for the phenomenon that salt crystallization damage develops preferentially in the free surface and corner areas.

4.3. Coupling effect between pore structure and crystallization

The crystallization infilling degree determines the effective range of the crystallization pressure on the pore wall. At low infilling degrees, the contact area between the crystal and the pore wall is limited, and the CSCF increases slowly; as the crystal growths further, the contact area expands, and the CSCF increases rapidly, thus showing a significant nonlinear response. At the same time, the crystallization pressure determines the maximum tensile stress. When both high infilling degree and high crystallization pressure occur together, the two effects superimpose, further increasing the maximum tensile stress. The pore spacing effects the spatial extent of the local stress field. When the distance between adjacent pores is small, the stress fields interfere with each other, but as the distance increases, their influence rapidly diminishes; after the boundary size reaches a certain range, a similar stable trend is also observed. Therefore, the stress concentration induced by NaCl crystallization exhibits distinct localized characteristics. Its amplitude is determined jointly by the crystallization state, pore structure, and external constraints, while the interactions between pores mainly occur

within a limited space.

4.4. FEA-driven machine learning method

The above results are generally consistent with existing studies, but they have further expanded the parameter range that can be described by the traditional crystallization pressure model and empirical relationships. The experimental results of Lee and Kurtis indicate that the damage caused by salt crystallization is significantly affected by the pore structure of the material [12]. Yang et al. further pointed out that the continuous accumulation of salt will cause the induced crystallization tensile stress to gradually increase [15]. This paper provides a mechanical explanation for the aforementioned pore structure effects and salt accumulation effects from two aspects: pore geometric stress concentration and the contact range between the crystal and the pore wall.

The existing pore-scale models also indicate that NaCl crystallization can generate significant tensile stress at the pore tips. Based on this, empirical relationships were established using pore aspect ratio, infilling degree, and crystallization pressure. This paper further considered pore spacing, boundary size, and boundary type, and it became even more evident that the limitations of the traditional empirical relationships were more prominent. The FEA-driven machine learning model does not require specifying the specific formula form of the relationships between variables in advance. The BPNN achieved an the R^2 of 0.992 on the independent test set and could simultaneously reproduce the nonlinear response of infilling degree, the nearly linear effect of crystallization pressure, the scale effect of pore spacing, and the significant differences between different boundary conditions. More importantly, SHAP and response surface analysis re-transform this predictive relationship into interpretable parameter contributions and interaction relationships, identifying boundary conditions, infilling degree, crystallization pressure and pore morphology as the main sensitive factors.

More importantly, the role of machine learning in this article is not to replace physical models, but to expand the traditional preset empirical formulas into proxy descriptions that can handle multiple parameters, nonlinearity, and category boundary conditions. FEA simulation provides the data foundation under mechanical constraints, machine learning is responsible for reconstructing the multi-dimensional response relationships, and interpretability analysis is used to verify whether these relationships are consistent with the finite element laws and existing physical understanding. This

combination enables the complex relationships among crystallization pressure, pore structure and spatial constraints to be quantitatively described within a unified framework.

4.5. Modeling limitations and engineering insights

This paper still adopts the two-dimensional idealized dual-pore model and homogeneous linear elastic assumptions. Therefore, it mainly describes the local stress response before crack initiation, and cannot directly simulate the crack propagation and stress release in the actual three-dimensional pore network. Furthermore, the crystallization pressure and infilling degree are currently treated as independent inputs and have not yet been directly coupled with water-salt transport, solution supersaturation, and crystal growth kinetics. The effectiveness of the machine learning model is also limited by the current restricted parameter space of the FEA. Further studies can incorporate real three-dimensional pore structures, transmission-crystallization coupling and fracture models to achieve continuous prediction from environmental effects to local cracking.

The results of this study indicate that the risk of salt crystallization damage cannot be solely assessed by the crystallization pressure or the macroscopic tensile strength of the material. It also depends on the crystallization state, pore geometry, and local mechanical constraints. In particular, the combination of a high infilling degree, sharp pores, and unfavorable boundary constraints is more likely to result in higher local tensile stress. It can be predicted that enhancing the surface properties [39] or reinforcing the micro cracks [40] are expected to improve the material's resistance to crystallization pressure-induced damage and failure. This work holds significant scientific and engineering value for the study of the evolution and improvement of the performance of civil engineering materials in salt erosion environments, and lays the foundation for the development of micro-mechanics machine learning research in engineering materials.

5. Conclusions

This article combines micropore-scale FEA with interpretable machine learning methods to study the crystallization stress concentration induced by the confined crystallization of NaCl within micropores of hardened cement paste surface, and systematically analyzes the combined effects of pore structure, crystallization state, and boundary conditions. The main conclusions are as follows:

(1) The crystallization pressure of NaCl can significantly amplify the local tensile stress at the pore tip. The maximum tensile stress mainly occurs at the end of the long axis of the elliptical pores, and the high-stress area is concentrated in the vicinity of the pores. Under fully infilled conditions, the maximum tensile stress under different boundary conditions can reach 17.88 times the crystallization pressure, indicating that the crystallization pressure can undergo significant local stress concentration after being affected by the pore geometry and spatial constraints.

(2) Pore morphology, crystal infilling, and crystallization pressure are the main continuous variables that control local tensile stress. The maximum tensile stress increases with the increase of the pore aspect ratio, and it shows a nearly linear relationship with the crystallization pressure. However, it exhibits a significant non-linear acceleration feature with the increase of the infilling degree; in contrast, the influence of the crystal aspect ratio is relatively weak. Adjacent pores only show significant stress coupling at a relatively small spacing. As the pore spacing and boundary size increase, their influence gradually weakens.

(3) Spatial boundary constraints are the key factor in regulating the stress concentration. The type of boundary conditions has a significantly greater impact on the maximum tensile stress than the boundary size itself. Different constraint states result in significantly different stress responses. The essence of its effect lies in changing the deformation constraints and stress transfer paths of the matrix around the pores, indicating that the spatial position of the pores is an unignored factor when evaluating the local damage risk of salt crystallization.

(4) FEA-driven machine learning can effectively represent the multi-factor nonlinear relationships that traditional empirical formulas are unable to describe. The BPNN prediction achieved an R^2 of 0.992, RMSE of 0.302 MPa, and MAE of 0.148 MPa on the independent test set, and could reproduce the finite element responses under different crystallization pressures, infilling degrees, pore morphologies, and boundary conditions. Compared with the empirical relationships in the form of preset functions, machine learning models can further identify the boundary effects, scale effects, and the nonlinear interactions between pore structure and infilling degree, thereby establishing a unified quantitative connection between crystallization, pore structure and spatial constraints and local maximum tensile stress. This research work holds significant scientific and engineering value for the performance evolution and improvement study of civil engineering materials in salt erosion environments.

CRediT authorship contribution statement

Xuefeng Liu: Methodology, Investigation, Software, Visualization, Writing - Original Draft, Writing - review & editing; **Ze Zhang**: Methodology, Investigation, Software, Visualization, Writing - Original Draft, Writing - review & editing; **Jinbo Yang**: Supervision, Project administration, Funding acquisition, Conceptualization, Methodology, Investigation, Writing - Original Draft, Writing - review & editing; **Siqi Li**: Methodology, Investigation, Software, Visualization, Writing - Original Draft, Writing - review & editing; **Zhenhua Huang**: Methodology, Investigation, Software, Visualization; **Jinpeng Zhang:** Supervision, Project administration.

Declaration of competing interest

The authors declare that they have no known competing financial interests or personal relationships that could have appeared to influence the work reported in this paper.

Acknowledgment

The financial support for ongoing project by the Natural Science Foundation of Shandong Province (ZR2023ME039) is greatly acknowledged.

Data availability

The data are available from the corresponding author on reasonable request.

References

[1] X.Q. Chen, H.F. Yu, C.Y. Wu, W.H. Chen, H.Y. Ma, H.F. Zhang, Study on the salt corrosion resistance and structural performance of basic magnesium sulfate cement concrete, Constr. Build. Mater. 537 (2026) 13.

[2] X. Meng, J.H. Mao, Y.D. Xu, Z. Chen, Y. Liu, Y. Zeng, D. Meng, Insights into the crystal nucleation of Friedel's salt (FS) under electric fields from experiments and molecular dynamics simulations, Appl. Surf. Sci. 747 (2026) 14.

[3] X. Qiu, W.Z. Chen, J.Q. Yuan, X.J. Tan, G.J. Wu, W.S. Zhao, Characteristics of pore structure evolution of ferrite-rich sulfoaluminate cement grouting materials under seawater corrosive environment, J. Clean Prod. 566 (2026) 10.

[4] Z.Q. Liu, G. De Schutter, D.H. Deng, Z.W. Yu, Micro-analysis of the role of interfacial transition zone in "salt weathering" on concrete, Constr. Build. Mater. 24(11) (2010) 2052-2059.

[5] S. Razki, F. Benboudjema, A. Bourdot, S. Langlois, A. Fau, F. Hafid, T. Honorio, Crystallization pressure in ASR expansion quantified by thermodynamic modeling and micromechanics, Cement and Concrete Research 193 (2025) 107878.

[6] M.H. Alyami, H. Mosavi, R.S. Alrashidi, M.A. Almarshoud, C.C. Ferraro, K.A. Riding, Lab and Field Study of Physical Sulfate Attack on Concrete Mixtures with Supplementary Cementitious Materials, J. Mater. Civ. Eng. 33(1) (2021) 14.

[7] Q. Wang, W. Wilson, K. Scrivener, Unidirectional penetration approach for characterizing sulfate attack mechanisms on cement mortars and pastes, Cement and Concrete Research 169 (2023) 11.

[8] H. Wang, Z. Liang, Y. Song, Z. Wu, Q. Yang, G. Xu, A physics-informed digital design framework to enhance freeze–thaw durability of engineered concrete: A case study on basalt fiber concrete, Advanced Engineering Informatics 76 (2026) 104972.

[9] Lei Shen, Weigang Zhao, Hao Yin, Lei Gan, Hao Gu, Mingyuan Zhu, Giovanni Di Luzio, Gianluca Cusatis, Discrete hygro-thermo-mechanical coupled modeling of concrete under freeze-thaw cycles: Cracking pattern, mechanical degradation and external load effect, Comput. Meth. Appl. Mech. Eng. 463, Part A(2027) 119338.

[10] Y. Yi, D.J. Zhu, S.C. Guo, Z.H. Zhang, C.J. Shi, A review on the deterioration and approaches to enhance the durability of concrete in the marine environment, Cem. Concr. Compos. 113 (2020) 14.

[11] X.B. Zuo, Z.K. Zheng, X.N. Li, Y.X. Zou, L. Li, Mesoscale numerical simulation on the deterioration of cement-based materials under external sulfate attack, Eng. Fail. Anal. 151 (2023) 107419.

[12] B.Y. Lee, K.E. Kurtis, Effect of pore structure on salt crystallization damage of cement-based materials: Consideration of w/b and nanoparticle use, Cement and Concrete Research 98 (2017) 61-70.

[13] X. Jiang, S. Mu, J.P. Liu, Influence of chlorides and salt concentration on salt crystallization damage of cement-based materials, Journal of Building Engineering 61 (2022).

[14] H.F. Sun, S.R. Yang, Q. Li, Y.X. Chen, Z.M. Zhou, J. Bai, Y.C. Wang, Influence of the exposure condition on the physical salt attack to cementitious materials under marine environment, Constr. Build. Mater. 533 (2026) 11.

[15] J. Yang, Z. Zhang, Y. Zhang, Effects of temporal salt accumulation during accelerated drying-wetting cycles on physical properties of cement mortars and determining of ocean salt crystallization pressure stress, Next Materials 9 (2025) 101083.

[16] M. Zhang, S.S. Qin, H. Lyu, C.Y. Chen, D.J. Zou, A. Zhou, Y. Li, T.J. Liu, A transport-chemical-physical-mechanical model for concrete subjected to external sulfate attack and drying-wetting cycles, Eng. Fract. Mech. 293 (2023) 17.

[17] Z. Zhang, J.B. Yang, Y. Zhang, Numerical Simulation of Sodium Chloride Crystallization Pressure in Micro Pores of Hardened Cement Paste, JOURNAL OF THE CHINESE CERAMIC SOCIETY. 53(2) (2025) 313-324. (In Chinese)

[18] N. Lo Presti, A.M. D'Altri, L. Patruno, G. Castellazzi, H. Derluyn, S. de Miranda, Multiscale simulation of salt crystallization-induced damage in porous materials, Materials and Structures 58(6) (2025) 23.

[19] M. Koniorczyk, D. Gawin, Modelling of salt crystallization in building materials with microstructure - Poromechanical approach, Constr. Build. Mater. 36 (2012) 860-873.

[20] G. Castellazzi, A.M. D'Altri, S. de Miranda, H. Emami, L. Molari, F. Ubertini, A staggered multiphysics framework for salt crystallization-induced damage in porous building materials, Constr. Build. Mater. 304 (2021) 13.

[21] J. Zhang, Y.M. Lai, J.F. Li, Y.H. Zhao, Study on the influence of hydro-thermal-salt-mechanical interaction in saturated frozen sulfate saline soil based on crystallization kinetics, Int. J. Heat Mass Transf. 146 (2020) 14.

[22] J. Choo, W.C. Sun, Cracking and damage from crystallization in pores: Coupled chemo-hydro-mechanics and phase-field modeling, Comput. Meth. Appl. Mech. Eng. 335 (2018) 347-379.

[23] S. Khani, D. Conciatori, L. Chouinard, Modeling the Time-Dependent Variation of Road Salt Concentrations Using Analytical and Machine-Learning Approaches to Advance Service Life Predictions for Concrete Structures, Transp. Res. Record 2679(3) (2025) 1005-1020.

[24] W. Zhang, Z.H. Duan, C. Liu, Y.Z. Yao, H.W. Liu, A. Nasr, Z.P. Zhu, Z.N. Zhang, Performance optimisation and predictive modelling of rice husk ash recycled concrete under the coupled action of freeze-thaw cycles and chloride erosion: Experimental study and machine learning, Constr. Build. Mater. 481 (2025) 17.

[25] W.G. Chen, Y.F. Liu, L. Liang, Z.H. Xue, Z. Basang, C. Shi, J.T. Yu, K.Q. Yu, Machine learning-powered inverse design for 3D-printable engineered cementitious composites (3DP-ECC): Advancing insights into rheological properties, Cement and Concrete Research 209 (2026) 37.

[26] H. Wang, J.L. Lin, Y.C. Miao, L.G. Wang, R. Liang, Z.Y. Lu, J.Y. Jiang, Hydrogel-guided dispersion strategy for enhancing the toughening efficiency of liquid polymers in cement paste, Cement and Concrete Research 195 (2025) 11.

[27] F. Yu, D.Q. Sun, M.J. Hu, J. Wang, Study on the pores characteristics and permeability simulation of pervious concrete based on 2D/3D CT images, Constr. Build. Mater. 200 (2019) 687-702.

[28] X.F. Wang, Z.J. Yang, J.R. Yates, A.P. Jivkov, C. Zhang, Monte Carlo simulations of mesoscale fracture modelling of concrete with random aggregates and pores, Constr. Build. Mater. 75 (2015) 35-45.

[29] W. She, G.T. Zhao, D.G. Cai, J.Y. Jiang, X.Y. Cao, Numerical study on the effect of pore shapes on the thermal behaviors of cellular concrete, Constr. Build. Mater. 163 (2018) 113-121.

[30] A. Naillon, P. Joseph, M. Prat, Ion Transport and Precipitation Kinetics as Key Aspects of Stress Generation on Pore Walls Induced by Salt Crystallization, Phys. Rev. Lett. 120(3) (2018) 5.

[31] W. Guo, Y. Wei, Investigation of compressive creep of calcium-silicate-hydrates (C-S-H) in hardened cement paste through micropillar testing, Cement and Concrete Research 177 (2024) 107427.

[32] S.J. Chen, W.H. Duan, Z.J. Li, T.B. Sui, New approach for characterisation of mechanical properties of cement paste at micrometre scale, Mater. Des. 87 (2015) 992-995.

[33] X.D. Chen, S.X. Wu, J.K. Zhou, Experimental and modeling study of dynamic mechanical properties of cement paste, mortar and concrete, Constr. Build. Mater. 47 (2013) 419-430.

[34] K. Fuenkajorn, D. Phueakphum, Effects of cyclic loading on mechanical properties of Maha Sarakham salt, Eng. Geol. 112(1-4) (2010) 43-52.

[35] Z.Q. Liu, D.H. Deng, G. De Schutter, Z.W. Yu, Micro-analysis of "salt weathering" on cement paste, Cem. Concr. Compos. 33(2) (2011) 179-191.

[36] A. Naillon, P. Joseph, M. Prat, Ion Transport and Precipitation Kinetics as Key Aspects of Stress Generation on Pore Walls Induced by Salt Crystallization, Phys. Rev. Lett. 120(3) (2018) 5.

[37] J.B. Yang, P. Zhang, A concise pore structure model for predicting the effective ion diffusion coefficients of cementitious materials, Constr. Build. Mater. 265 (2020) 4.

[38] J. Rezaeepazhand, M. Jafari, Stress concentration in metallic plates with special shaped cutout, International Journal of Mechanical Sciences 52(1) (2010) 96-102.

[39] J.B. Yang, Y. Zhang, Z. Zhang, Research on initial external solution curing technology to enhance durability of cement mortars and chemical deposit infilling mechanism, Innovative Infrastructure Solutions 11(7) (2026) 355.

[40] X.F. Liu, J.P. Zhang, J.B. Yang, F.J. Yang, M.X. Niu, Influence of slurry expansion properties on the mechanical behavior and failure characteristics of slurry-coal cemented body, Constr. Build. Mater. 541 (2026) 16.